Ultra-strong nanotwinned Al-Ni solid solution alloy with significant plasticity

Journal:	*Nanoscale*
Manuscript ID	NR-ART-06-2018-005139.R1
Article Type:	Paper
Date Submitted by the Author:	15-Oct-2018
Complete List of Authors:	Zhang, Yifan; Purdue univsersity, School of Materials Engineering Li, Qiang; Purdue University , School of Materials Engineering xue, sichuang ; Purdue University System, School of Materials Engineering Ding, Jie; Purdue univsersity, School of Materials Engineering Xie, Dongyue; University of Nebraska-Lincoln, Mechanical and Materials Engineering Li, Jin; Purdue University, School of Materials Engineering Niu, Tongjun; Purdue University , School of Materials Engineering Wang, Han; Purdue University, School of Materials Engineering Wang, Haiyan; Purdue University System, School of Materials Engineering; Purdue University, School of Electrical and Computer Engineering Wang, Jian; University of Nebraska-Lincoln Zhang, Xinghang; Purdue University System, School of Materials Engineering

Ultra-strong nanotwinned Al-Ni solid solution alloy with significant plasticity

Y.F. Zhang[a], Q. Li[a], S, Xue[a], Jie Ding[a], D.Y. Xie[c], Jin Li[a], Tongjun Niu[a] Han Wang[a], Haiyan Wang [a,b],

*J. Wang[c] and X. Zhang[a]**

[a] *School of Materials Engineering, Purdue University, West Lafayette, IN 47907, United States*

[b] *School of Electrical and Computer Engineering, Purdue University, West Lafayette, IN 47907,*

[c] *Mechanical and Materials Engineering, University of Nebraska-Lincoln, Lincoln, NE 68588*

Abstract

Twin boundaries have been proven effective to strengthen metallic materials while maintaining plasticity. Al, however, has low twinning propensity due to its high stacking fault energy. Here we show, by using a small amount of Ni solutes, high-density twin boundaries and stacking faults form in sputtered Al-Ni solid solution alloys. First-principle density function theory calculations show that Ni solute facilitates the formation of stacking faults and stabilizes nanotwins in Al-Ni solid solutions. *In-situ* micropillar compression studies reveal high flow stress (exceeding 1.7 GPa), comparable to high strength martensitic steels and Ni alloys. Furthermore, significant plasticity was observed in these nanotwinned Al-Ni alloy films due to the existence of high density twin boundaries and 9R phase.

Key words: High-strength Al alloy, nanotwins, in-situ micropillar compression, 9R phase

*Corresponding Author; Email: xzhang98@purdue.edu

Introduction

Al alloys have wide spread applications in automobile and aerospace industry. However, the strength of most commercial Al alloys is low, less than 700 MPa. Various approaches have been used to strengthen Al alloys, including age hardening [1,2] and severe plastic deformation (SPD) etc. [3–5], and nanocomposites[6,7]. However, the strength of most advanced Al alloys remains limited with few exceptions. The combination of high pressure torsion and age hardening leads to ultra-high strength Al alloys, with flow stress approaching 1 GPa[8].

Twin boundaries (TBs) have been shown to strengthen various metallic materials that have low stacking fault energy (SFE), such as Cu (SFE of ~ 40mJ/m^2)[9,10], Ag(~16 mJ/m^2)[11], and stainless steels (20-50 mJ/m^2) [12,13]. Extensive studies have shown nanotwinned (nt) metals with high-density Σ3 (111) coherent twin boundaries (CTBs) may have high strength and ductility[14–17], as well as thermal stability [18,19]. Molecular Dynamics (MD) simulations [20–22] and experimental studies[13,23–25] confirmed that CTBs act as strong barriers to dislocation transmission because of the slip discontinuity across CTBs. *In-situ* nanoindentation and tension studies have also shown that TBs can introduce work hardening in metallic materials [26–30]. Meanwhile, CTBs can accommodate plasticity by acting as nucleation sites for dislocations [21,22,24] and enabling the symmetrical slip across CTBs[31].

Twinning propensity in Al is low due to its high SFE (120-166 mJ/m^2) [32]. Deformation twins have been observed sporadically in Al under extreme conditions, such as cryogenic ball milling [33], indentation of nanocrystalline Al [32] and high strain rate deformation [34–36]. Bufford *et al* [37] introduced growth twins into Al via a (Ag) template method by using magnetron sputtering. Xue

et al [38] synthesized ultra-fine-grained Al thin films with ~ 9% of twinned grains. They also showed that {112} textured Al films have the highest twin density comparing to other textured Al films [39]. Recently, Li *et al* [40] reported high-strength and ductile nt Al-Fe alloys. High-density Σ3{112} incoherent twin boundaries (ITBs) and 9R phase and nanoscale columnar grains lead to high flow stress (~1.5 GPa) and good deformability in the sputtered Al-Fe solid solution alloys. However, it is unclear if the high strength and nanotwins can be accomplished in other binary Al alloys.

Magnetron sputtering has been chosen to fabricate nanotwinned Al-Ni alloys. Other deposition techniques, such as atomic layer deposition (ALD)[41–43], and electrodeposition[44] have been used to fabricate Al or Al alloys. ALD of Al requires the usage of some precursors like trimethylaluminum, which needs to be handled with extremely care due to their pyrophoricity. In addition, nearly 1-3 %impurity atoms (e.g. carbon) are usually left in Al films during ALD deposition process[42]. Also, though ALD has been used to fabricate transition metals such as Co Cu and Ni [41,45–47], its deposition rate is very low, and we need micron thick films for nanomechanical testing. For similar safety reasons, electrodeposition of Al is not ideal either. For example, anhydrous aluminum chloride ($AlCl_3$)[44], also known as a neurotoxin, has been utilized to fabricate Al alloys.

In comparison, magnetron sputtering has been selected to deposit Al-Ni alloys for the following reasons. (i) It is a simple and environmental benign technique and free from usage of hazardous materials. (ii) Magnetron sputtering, operated at room temperature, has relative high deposition rate ~0.8 nm/s for Al, necessary to achieve a thicker coating for nanomechanical testing. (iii) The chemistry of Al alloys can be precisely controlled by adjusting deposition power via co-sputtering. (iv) Sputter-deposited films have high surface quality and low porosity.

In this work, we fabricated high-strength nt Al solid solution alloys by adding a small amount of Ni solute. Using first-principle density function theory calculations, we show that Ni solute facilitates the formation of stacking faults and stabilizes nanotwins in Al-Ni solid solutions. These nt Al-Ni solid solution alloys have harnesses exceeding 6 GPa, comparable to martensitic steels [48] or Ni alloys[49] and higher than high-strength age hardened Al alloys. *In-situ* micropillar compression experiments show these nt Al-Ni alloys have high flow stresses exceeding 1.7 GPa and remarkable plasticity. This study supports the motivation of using nanotwins and 9R phase to significantly strengthen Al alloys while maintaining their plasticity.

Experimental methods

At room temperature, 1.6-μm-thick Al-Ni films with seven different Ni compositions (2.2-11.7 at. %) were deposited on HF etched Si (111) substrates by DC magnetron sputtering using Al (99.99%) and Ni (99.99%) targets. Base pressure of the vacuum chamber was below 8×10^{-9} torr before depositions. During sputtering process, the Ar pressure was kept at 2×10^{-3} torr. To examine the microstructure of the films, out-of-plane θ-2θ scans and pole figure analysis were performed on a Panalytical Empyrean X'pert PRO MRD diffractometer. Transmission electron microscopy (TEM) studies were performed on a FEI Talos 200X analytical microscope operated at 200 kV. Energy dispersive spectroscopy (EDS) on FEI quanta 3D FEG scanning electron microscope was used to determine the composition of the Al-Ni films. Hardness and modulus of the Al-Ni films were measured by a Hysitron TI Premier nanoindenter at different indentation depths [50]. To avoid the substrate effect, maximum indentation depths were no more than 240 nm (15% of the total film thickness). The focused ion beam (FIB) technique was used to fabricate micropillars with 700 nm

in diameter and a height-to-diameter aspect ratio of 2:1. FIB ion beam, though has its limitation[51], has been widely used to fabricate nanoscale samples used for in-situ nanoscale mechanical tests[51–54]. And the aspect ratio, pillar shape, surface morphology, tapering angle can be precisely tailored by adjusting FIB parameters. To avoid elastic or plastic buckling and deformation instability, the widely-adopted aspect ratio (pillar height to pillar diameter) is 2 to 6[53,55], and the ratio of 2 is the well-accepted and widely used value to achieve a reliable measurement of strength and plasticity. When the aspect ratio is much greater than 6, misalignment and buckling could render experimental results unreliable and unrepeatable. *In-situ* pillar compression tests were conducted inside a FEI quanta 3D FEG scanning electron microscope, by using a Hysitron PI 88xR PicoIndenter equipped with a 5-μm diamond flat punch tip. The deformed pillars were cut and thinned by using FIB to 100-150 nm in thickness before performing post-compression TEM analyses.

Results and discussion

Microstructure characterization

X-ray diffraction profiles in Fig. 1a show the formation of as-deposited Al-Ni single-phase solid-solution alloys. When the Ni composition is 4.5 at. % or less, the Al-Ni films have weak {111} texture (also see supplementary Fig. S1). Increasing the Ni composition to 9.3 at. % leads to a much stronger {111} texture. XRD pole figure analysis in Fig1b indicates the existence of high density growth twins in textured Al-Ni films. Plan-view TEM image in supplementary Fig. S2 shows that these Al-Ni thin films have polycrystalline grains. As shown in Fig. 1c, the average grain sizes derived from statistics of grain size distributions (Fig. S3) decrease sharply from 130 ± 38 nm (for Al-2.2Ni) to 7 ± 3 nm (for Al-9.3Ni). The sputtered Al-Ni alloys have high hardness, varying from 4.37 ± 0.15 GPa for the Al-2.2 Ni to 6.43 ± 0.07 GPa for the Al-7.8 Ni alloy, and the

hardness reaches a plateau, ~ 6.4 GPa, thereafter. The harnesses as a function of $d^{-1/2}$ obtained from this work and literature are compiled in Fig1. d. The horizontal dash line denotes the hardness of the monolithic Al thin film (~0.7 GPa). The harnesses of bulk Al alloys are measured by microhardness test or converted by multiplying flow stress by a Tabor factor of 2.7[56] .

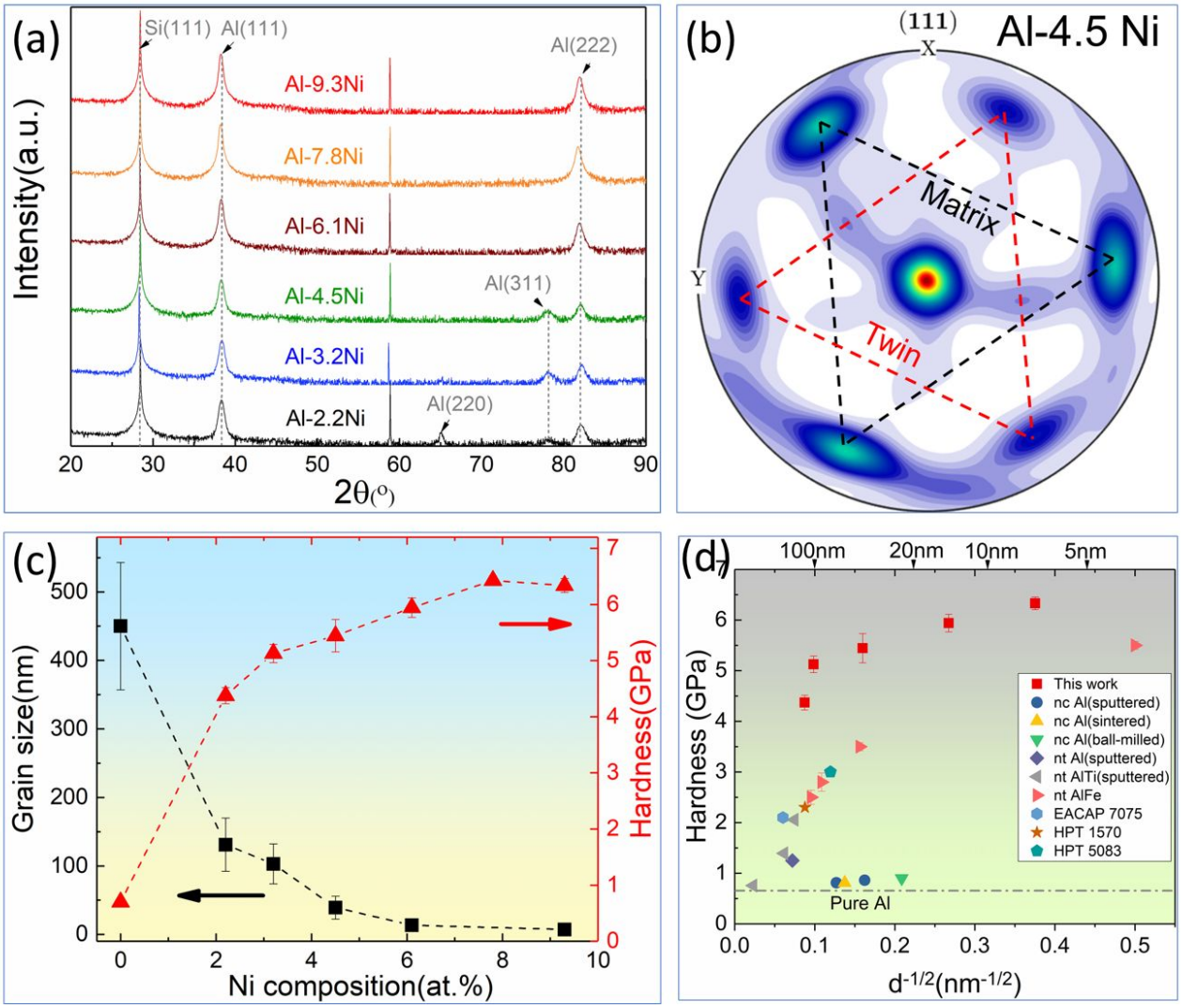

Fig 1. Evolutions of microstructures and hardness of Al-Ni alloys with Ni compositions. (a) The XRD profiles of sputtered Al-Ni solid solution alloy films with different Ni compositions. (b) XRD (111) pole figure analysis of the Al-4.5Ni thin films.; (c) The average grain sizes and indentation hardness vary with increasing Ni compositions. (d) Comparisons of hardness as a function of $d^{-1/2}$ for Al-Ni alloys with literature data on nt Al-Fe alloy[40], nt Al-Ti alloys[57], twinned Al[37], and nanocrystalline Al[58–60]and bulk Al alloys[8,61,62].

Microstructures of the as-deposited Al-Ni films were examined in cross-section TEM (XTEM) micrographs from the Al <110> zone axis. Bright-field and dark-field XTEM images (Fig.2(a_1)-(a_2)) of the as-deposited Al-4.5 Ni film depict columnar grains with an average diameter of 39 nm. The inserted SAD pattern indicates the formation of twins inside the polycrystalline Al-4.5Ni film. High-resolution TEM (HRTEM) micrographs (Fig.2(a_3) – (a_4) and supplementary Fig.S4) show several types of typical grain boundaries in the Al-4.5Ni film. The growth direction is denoted by white arrows. Fig.2(a_3) and the inserted fast Fourier transform (FFT) present the frequently observed diffuse ITBs (or 9R phase), which are parallel to the growth direction. Inclined CTBs (nearly parallel to the growth direction) marked as a red dash line in Fig.2(a_4) were also observed. Fig.S4 shows a high angle grain boundary with a misorientation angle of 19^o. Similar TEM analyses of the Al-6.1Ni film in Fig.2(b_1) -(b_2) show stronger {111} texture and smaller average grains than the Al-4.5Ni alloy. Compared with Al-4.5Ni, the Al-6.1Ni has a higher density of ITBs and 9R phase as shown in Fig. 2(b_3) and Fig.2(b_4).

In comparison to the Al-4.5 Ni and Al-6.1Ni films, the as-deposited Al-9.3Ni alloy has even finer columnar grains (Fig. 2(c_1), (c_2)), with strong {111} texture and high-density twins, as evidenced by the single-crystal like twinned diffraction pattern. The grain size of the as-deposited Al-9.3Ni increases along the growth direction, with finer grains (~3nm) near the film-substrate interface and coarser ones (~10 nm) close to the film surface. The HRTEM image in Fig. 2(c_3) shows the diffuse ITBs between two columns and scattered highly-distorted regions (in blue dotted squares). A processed HRTEM micrograph in Fig.2(c_4) shows the formation of discontinuous 9R phase in nanoscale columns. Statistics in Fig. S5 also shows that the fraction of columns with 9R increase from 27% (Al-4.5Ni) to 52%(Al-9.3Ni).

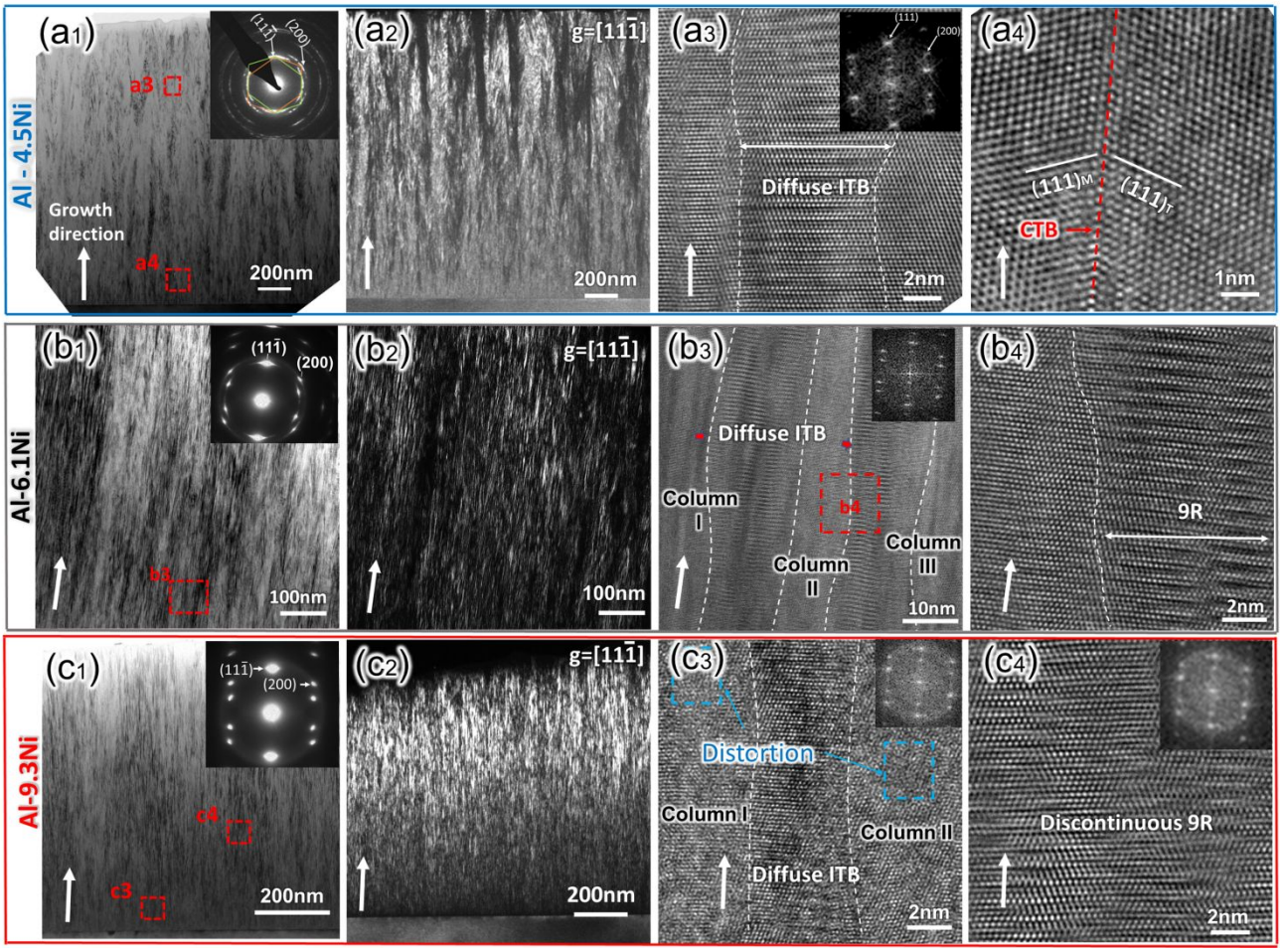

Fig. 2. Cross-section TEM(XTEM) studies on the microstructures of as-deposited Al-Ni alloys. (a_1-a_2) Bright-field and dark-field cross-section TEM (XTEM) images of Al-4.5Ni. of Al-4.5Ni and inserted SAD showing nanoscale polycrystalline columns. (a_2) Dark field cross section TEM image of Al-4.5Ni (a_3-a_4) Diffuse ITB in the film and inclined coherent twin boundary (CTB) in the matrix. (b_1-b_2) XTEM images of Al-6.1Ni demonstrates the formation of nanotwinned columnar grains. The inserted SAD pattern shows slight grain rotation (b_3) Three nano columns separated by two adjacent diffuse ITBs, where the region marked by the red dotted box is magnified in (b_4). (c_1-c_2) XTEM images of Al-9.3Ni film with the inserted SAD pattern indicating highly {111} twinned pattern. (c_3-c_4) Diffuse ITB and distortions in nanocolumns and intermingled 9R phase in columnar nanograins.

In-situ micropillar compression

In-situ micropillar compression tests were performed on selected Al-Ni alloys. Fig.3a-c reveal the morphology evolutions of pure Al, Al-4.5Ni and Al-9.3 Ni pillars tested to different strain levels. Multiple shear bands were observed in Al during deformation as shown in Fig. $3a_2$-a_4 (see supplementary video 1 for details). In contrast, during the compression tests of Al-4.5Ni (Fig. $3b_2$-b_4) and Al-9.3Ni (Fig. $3c_2$-c_4) micropillars, there is no sign of shear bands. A prominent feature of the Al-Ni alloy pillars is the significant deformation (dilation) near the top of the pillar. Prominent deformation zones initiated from the top of the pillars transmitted gradually downward to the lower portion of the pillars, leading to the reverse trapezoid shapes (Fig. $3b_4$ and Fig. $3c_4$). To calculate true stress-strain curves of the micropillars, real-time diameter changes near the top and bottom of the deformation zones were plotted as a function of displacement (supplementary Fig.S5). Also, several partial loading and unloading compression tests were carried out on the Al-4.5 Ni and Al-9.3 Ni pillars as shown in Fig.3d to estimate the elastic modulus of the pillars. Multiple tests were performed to check reproducibility of the tests. Load drift and substrate effect were also considered for the calculation of true stress and true strain [53]. As shown in Fig. 3d, the Al-4.5 Ni and Al-9.3Ni pillars have flow stress (measured at 8% strain) of 1.0 ± 0.1 GPa and 1.75 ± 0.1GPa, respectively, much greater than that of pure Al, ~ 0.26 GPa. Also, Al-4.5Ni and Al-9.3Ni have much higher work hardening rate than pure Al (Fig. 3e). The prominent difference of flow stress between the Al-4.5Ni and Al-9.3Ni will be addressed in the discussion and supplementary sections.

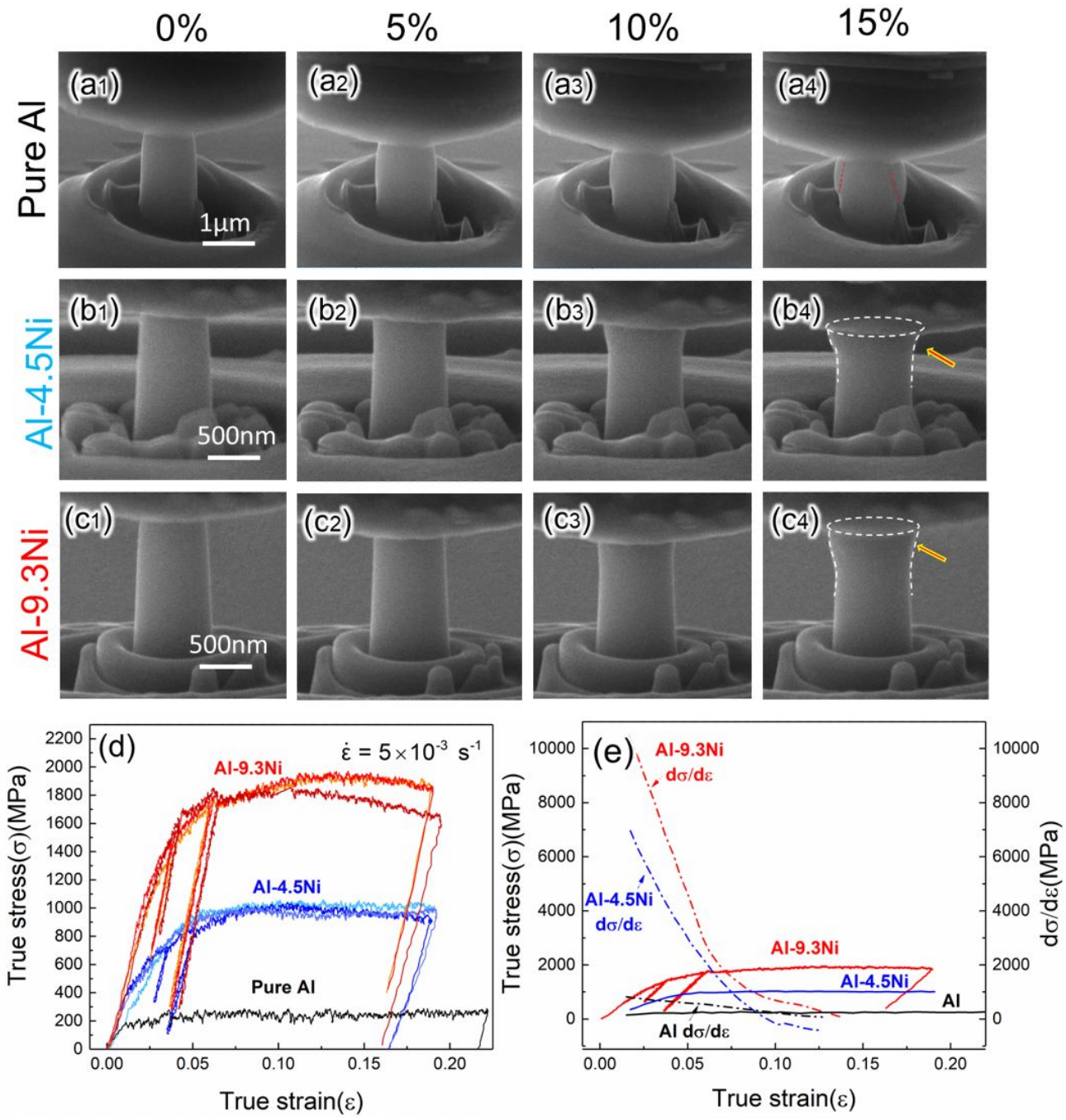

Fig. 3. *In-situ* micropillar compression studies of several Al-Ni alloy specimens. (a_1 - a_4) The morphology changes of pure-Al pillar during the compression test. (b_1 - b_4) Compression test of the Al-4.5Ni pillar shows the localized deformation near the top portion of the pillar. (c_1 - c_4) Substantial deformation near the top of the Al-9.3Ni pillar without evidence of shear band formation. (d) The comparison of true stress-strain curves shows significantly higher flow stress in Al-4.5Ni and Al-9.3Ni than monolithic Al. (e) Comparisons of the work hardening rate ($d\sigma/d\varepsilon$) of Al-9.3Ni, Al-4.5 Ni and pure Al.

Postmortem XTEM analysis

Fig. 4 shows the postmortem XTEM analysis of a deformed Al-9.3Ni pillar. The overview of the deformed pillar in Fig. 4a shows the clear dilation of the pillar top. Dark-field TEM image (Fig. 4.b) and the inserted SAD patterns taken at a depth of ~ 200, 400 and 600 nm underneath the pillar top surface confirm the grain rotation and detwinning near the top, and the retention of twins and 9R phase in lower portion of the largely unchanged pillar. Numerous locations of the deformed pillar were examined by using HRTEM micrographs. HRTEM images in Fig.4c-d taken near the top portions of the deformed pillar show prominent detwinning and grain coarsening. Although columnar grain boundaries were largely removed, distorted 9R patches are still visible (Fig. 4c), and residual dislocations, such as Frank partials are frequently observed (Fig. 4d). At a depth of ~ 200 nm underneath the region c-d. HRTEM micrographs (Fig. 4e-g) show prominent grain rotation, and the retention of columnar nanograins. The inserted FFTs in Fig. 4e and f show that 9R phase and nanotwins remain. The magnitude of grain rotations relative to the growth direction (white arrow) is labeled in the HRTEM micrographs.

The HRTEM micrograph taken at location h (Fig. 4h) shows the preservation of high-density nanocolumns and 9R phase in a region that was not prominently deformed. EDS maps of the deformed regions, ~ 300 and 500 nm from the pillar top surface (Fig.S7), show insignificant Ni segregation. The retention of few scattered ITB patches and nanotwins near the pillar top is also shown in the HRTEM micrograph in Fig.S8. The panoramic view of the microstructure of Al-Ni micropillar is depicted schematically in Fig.S9.

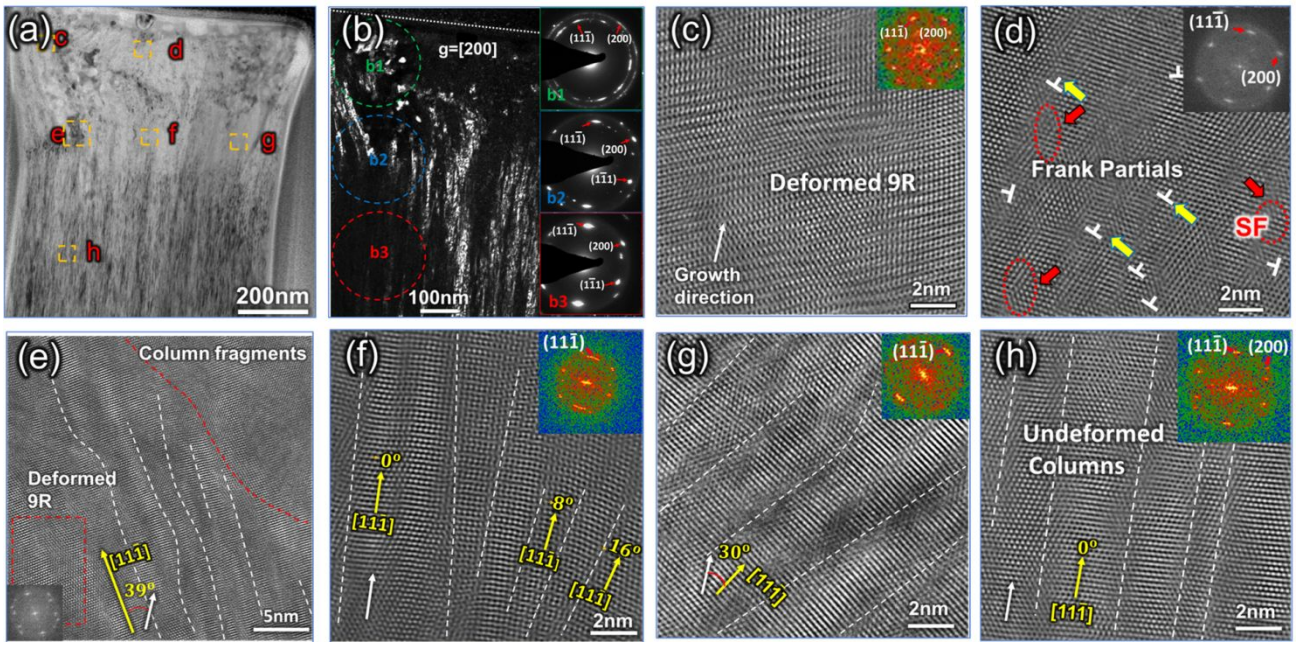

Fig.4. XTEM micrographs of a deformed Al-9.3Ni micropillar. (a) Low-magnification XTEM micrograph showing the overview of the deformed pillar. (b) Dark-field XTEM image of deformed pillar and inserted SAD patterns that taken from the pillar top (b1), medium (b2) and bottom (b3). (c) HRTEM image and FFT of the upper top portion of pillar (box b in Fig. 4a) indicate deformed 9R retentions (d) HRTEM micrograph shows the single-crystal-like area with Frank partial dislocations and stacking faults in the deformed central top portion of the pillar. (e) The magnified TEM image showing the boundary between the deformed vs. less deformed pillar. (f) HRTEM image taken from box f in Fig.4a demonstrates the initiation of grain rotation. (g) Inclined tiny columns in the right central portion of the deformed pillar. (h) HRTEM micrograph taken from the bottom portion of the pillar shows the retention of tiny twinned columns filled with diffused ITBs.

The formation of nanotwins and 9R in as-deposited Al-Ni solid solution alloys

Broad 9R phase and ITBs are rare in pure Al because of its high SFE. Xue *et al* have shown that high strain rate deformation can introduce 9R phase in sputtered ultra-fine grained Al film because ~ 9% of the grains in the as-deposited Al films contains incoherent twin boundaries (growth twins); and ITBs evolve rapidly into 9R during deformation [63]. Bufford *et al* show that the broad 9R phase can form in sputtered Al with the assistance of twinned Ag seed layer [37]. The local shear stress may also facilitate the formation of growth twins in Al [37].

In addition to these methods, solute may also facilitate the formation of 9R or growth twins in Al. It has been shown in Al-Fe that Fe solutes increase the energy barrier for migration of trailing partials, because the energy gap between stable and unstable SFE has been increased by Fe solute[40]. MD simulations have also shown that the 9R phase formed in Al-Fe is stable at room temperature, whereas 9R phase induced in Al by shear is unstable[63]. Ni solute plays a critical role in increasing the twinnability of Al. Using first-principle density function theory calculations, we studied the effect of Ni solute on the migration energy associated with surface atom clusters and stacking fault energies. The details are summarized in detail in supplementary information. The energy barrier associated with the migration of a surface heptamer from normal fcc to stacking fault position (Fig. 5a, c) increase from 0.064 eV (pure Al) to 0.089 eV (Al-Ni), and the energy barrier increases even more for a surface trimer. DFT calculations in Fig. 5b and d show that the addition of Ni solute (~3%) decreases the SFE of Al from ~120 to 112 mJ/m^2. Both factors promote the formation of TBs and 9R phase in Al.

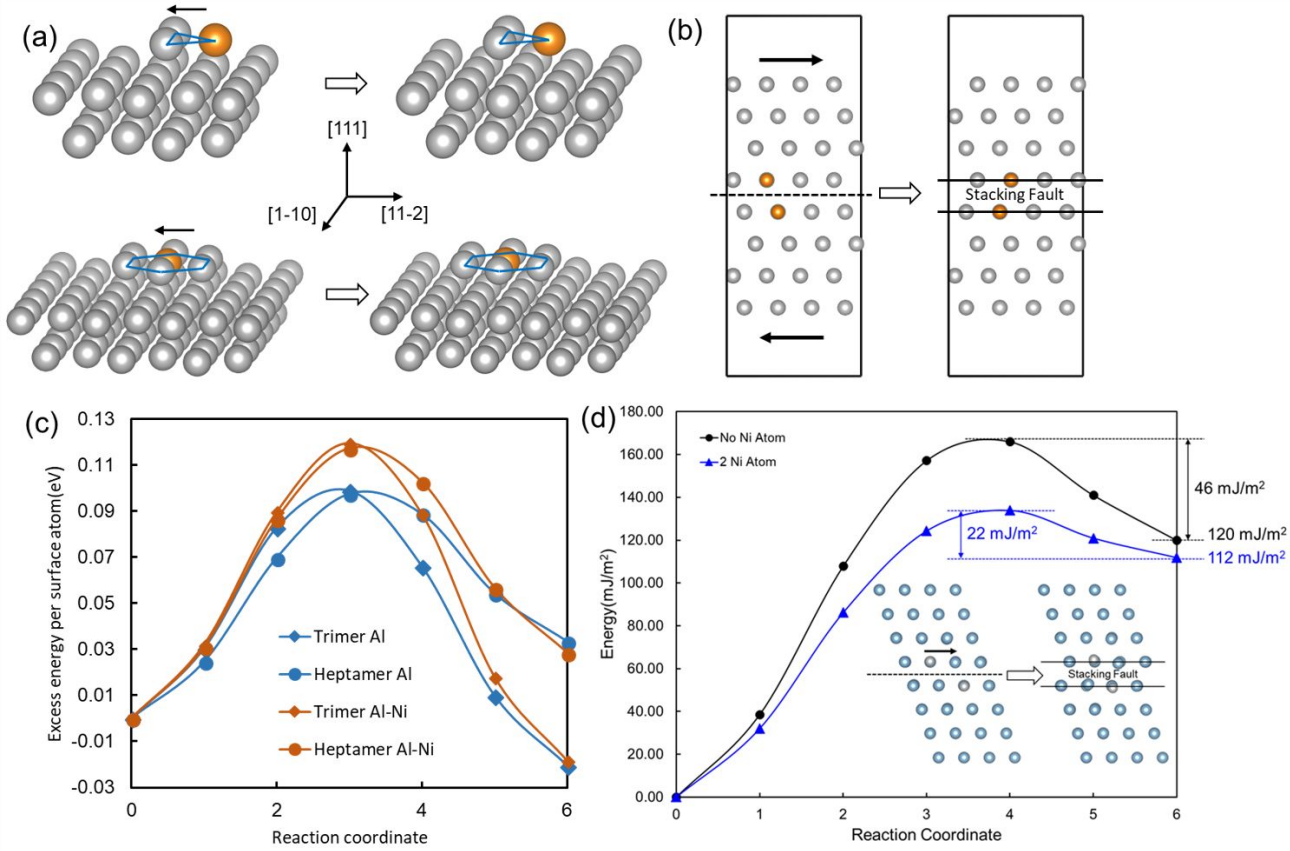

Fig.5 DFT calculation models and results. (a) Atomic configurations of surface trimer and heptamer used for first-principle density function theory (DFT) calculations. (b) Slab models and atomics configurations using to calculate SFEs. (c) The change in excess energy per surface atom with reaction coordinate. (d) The change in excess energy per unit area with reaction coordinate. The reaction coordinate 0 is corresponding to normal fcc structure and 6 represents the stacking fault structure.

Our previous studies show island coalescence during grain growth promotes the formation of TBs in Al films[38,39]. XTEM studies show the grain size of Al-Ni is in the range of 7-130 nm. TBs may form through coalescence of adjacent nanocolumns during the early stage of film growth [38,39]. Based on DFT calculations in Supplementary S3, Ni solutes prefer to become substitutional atoms in Al because of the lower formation energy, -0.94eV. Consequently, the Ni solutes may retard the diffusion of Al atoms, and thus increase nucleation rate of twins, resulting in a high TB density. As shown in Fig. 4, coalescences among {111} textured columns give rise to high-density

ITBs in as-deposited Al-9.3Ni films, while the CTBs and high-angle GBs form in the polycrystalline Al-4.5 Ni films. This observation suggests that the strong {111} texture also promote the formation of high-density TBs.

Detwinning occurs through collective glide of trailing partial dislocations [64]. However, Ni solutes may preserve TBs via retarding the detwinning process. The stress field surrounding Ni solutes (due to atomic size difference) may pin the glide of partial dislocations.

Mechanical properties

The sputtered Al-9.3Ni binary solid solution alloy has a high hardness of ~ 6.4 GPa and flow stress of ~1.7 GPa, comparable to high-strength nanocrystalline Ni films[65,66]. The high strength may originate from solid solution strengthening [67], grain size effect [68] and the introduction of high-density TBs and 9R phase [12,37,40]. The strengthening from these factors will be discussed in detail in the subsequent sections.

The solid solution effect can be estimated by using the Fleischer formula[69]

$$\Delta\tau = 0.0235 \cdot G_{solvent} \cdot \varepsilon_s^{3/2} \cdot c^n$$

where, $\Delta\tau$ is the shear stress, $G_{solvent}$ is the shear modulus of Al (26.9 GPa[70]), c is the concentration of solute atoms. ε_s is a factor that incorporates the distortion induced by changes in lattice parameter and shear modulus. n is a coefficient in the range of 0.5 - 1, and n = 0.5 for most coarse grained and ultrafine grained materials [66]. Modification should be made when applying the formula to nanocrystalline materials [66,68]. By using n = 0.75, the contribution of solid solution to hardening is estimated to be 1.4 GPa for 9.3% Ni. Clearly, the solid solution effect alone is insufficient to explain the remarkable hardening in the Al-Ni solid solution alloys.

Grain refinement is known to induce significant strengthening. However, as shown in Fig.1d, softening occurs with decreasing grain size. Previous studies [71,72] have also shown softening when grain size of nanocrystalline material is below a critical value. The breakdown of Hall-Petch effect [72] in nanocrystalline regime can be ascribed to several factors, such as the transition from dislocation dominated to grain boundary-mediated deformation mechanism. Both MD simulations and *in-situ* observations have revealed the stress-driven GB migration[73], GB rotation [74], as well as partial dislocation emission in nanocrystalline Al[75,76].

Next, we consider the influence of high-density ITBs and 9R phase on mechanical properties. To date, most prior studies focused on nt metals with a majority of CTB [9,20,22,49,77,78]. Both MD and experimental studies have shown that CTBs can effectively block the dislocation transmission [20,23,57,79,80], and introduce significant work hardening in metallic materials [26,27,29,81]. Furthermore, defective CTBs can accommodate plasticity by providing nucleation sites for full or Shockley partial dislocations [24].

However, few prior studies have focused on ITB-dominated strengthening in nt metals. Recently, both MD simulation and *in-situ* nanoindentation [30,40,82] studies have demonstrated the capability of ITBs to strengthening Al. *In-situ* nanoindentation studies on nt Al [30] showed dislocations pile up against ITBs, leading to substantial work hardening and distorted ITB. MD simulations also confirm that ITBs in Al effectively block the transmission of dislocations in Al. At higher applied stress, ~ 0.5GPa, ITB migration occurs via disconnection glide to accommodate plasticity[30].

The as-deposited nt Al-Ni alloys contain high-density ITBs and 9R phase. A recent MD simulation study [40] shows that in nt Al-Fe, the broad 9R phase can effectively resist the transmission of dislocation and lead to prominent strengthening. It is likely that the broad 9R phase

in nt Al-Ni alloys may also contribute to significant enhancement in strength [40]. Meanwhile, uniformly distributed Ni solutes may decrease TB mobility and stabilize the 9R phase due to the solute drag effect. A number of studies have been performed on solute drag effect on GBs [83–85]. By using MD simulation, Borovikov *et al* [86] proved that the migration of ITBs in Cu was significantly impeded by Ag solutes. W.A *et al*[87] also reported the pinning effect of Mg atoms on the grain boundaries in Al-Mg thin films. Recently, Li *et al* demonstrated the Fe solute drag effect on stabilization of TBs in Ag-Fe solid solution alloy[88].

In addition to strengthening, 9R phase and ITB migrations play an important role on the plasticity of the high-strength Al-Ni alloys. As confirmed by the postmortem TEM analysis, in the top portion of the deformed pillars, substantial grain coarsening and grain rotation occurred due to detwinning and ITB migration. Such events should lead to softening of the deformed pillar top, and consequently the top portion of the pillars accommodates significant plasticity.

Interestingly, in the regions underneath the deformed pillar top, high density nt columns and 9R phase retain. The high-strength measured from the micropillar compression tests is a combination of strain softening in the pillar top and strain hardening in the undeformed regions. The deformation induced dilations of pillars gradually propagate downwards and eventually the entire pillar may sustain large plastic deformation under high stresses. This type of gradual shift of strain softening into the hard, rigid portion of the same materials has important implications.

First, strain hardening due to forest dislocations is often exhausted in most metallic materials at moderate strain levels. Consequently, plastic instability occurs. Meanwhile strain softening has been frequently observed in ultra-fine grained materials where work hardening capability is exhausted during deformation, and plastic deformation is highly localized in shear bands [89–93]. 9R phase and TBs can provide an important mechanism for the materials to

continuously deform at higher stresses. Second, the 9R phase in nt Al-Ni alloys are important barriers to the transmission of dislocations, and hence prominent strengthening is observed. However, at higher stress, ITBs can migrate and consequently lead to detwinning or strain softening[30] . The lower portion of the pillar remains largely undeformed as there is little resolved shear stress to activate the migration of partials due to the strong {111} texture of the film. Inclined CTBs and high angle GBs in polycrystalline Al-Ni films (Al-4.5Ni) could provide slip planes with higher Schmid factor, leading to a lower yield strength and flow stress. Similarly, grain coarsening and grain rotation lead to the generation of dislocations on the inclined slip systems. Consequently, the resolved shear stress is able to drive detwinning in the lower portion of the pillars. The combination of strain hardening and strain softening in nt Al-Ni could be an important way to maintain high strength and plasticity simultaneously.

Conclusions

In summary, nt Al-Ni alloys with high-density ITBs and 9R phase were fabricated by using magnetron sputtering. The addition of Ni solute is proven to be effective in increasing twinnability, decreasing grain size, and stabilizing TBs and 9R in Al alloys. The texture of Al thin films can also be tailored by changing Ni composition. *In-situ* micropillar compression tests reveal that nt Al-9.3Ni solid solution alloys achieve high flow stress, ~1.7 GPa, and significant plasticity. The 9R phase and ITBs enable work hardening, and high stresses, the detwinning ability of 9R phase at high stresses leads to work softening, and thus nanotwins and 9R phase ensure significant plasticity in the high-strength Al-Ni alloys.

Acknowledgement

We acknowledge financial support from Depart of Energy-Office of Basic Energy Sciences (DOE Award number: DE-SC0016337). H. Wang acknowledges financial support from the Office of Naval Research (N0014-16-1-2778) program managed by Dr. Antti Makinen. J. Ding is supported by PRF 53741-ND10. J. Ding and X. Zhang also acknowledge partial support by DOE-Nuclear Energy under DE-NE0008549. Accesses to the DOE-Center for Integrated Nanotechnologies (CINT) at Los Alamos and Sandia National Laboratories and the Microscopy Centers at Purdue University are also acknowledged. Atomistic simulations were completed utilizing the Holland Computing Center of the University of Nebraska, which receives support from the Nebraska Research Initiative.

Conflicts of interest

There are no conflicts of interest to declare.

References

1 J. B. Clark, *Acta Metall.*, 1968, **16**, 141–152.

2 D. A. Porter, K. E. Easterling and M. Sherif, *Phase Transformations in Metals and Alloys, (Revised Reprint)*, CRC press, 2009.

3 G. Nurislamova, X. Sauvage, M. Murashkin, R. Islamgaliev and R. Valiev, *Philos. Mag. Lett.*, 2008, **88**, 459–466.

4 R. Z. Valiev, N. A. Krasilnikov and N. K. Tsenev, *Mater. Sci. Eng. A*, 1991, **137**, 35–40.

5 H. J. Jiang, C. Y. Liu, B. Zhang, P. Xue, Z. Y. Ma, K. Luo, M. Z. Ma and R. P. Liu, *Mater. Charact.*, 2017, **131**, 425–430.

6 L. Jiang, H. Wen, H. Yang, T. Hu, T. Topping, D. Zhang, E. J. Lavernia and J. M. Schoenung, *Acta Mater.*, 2015, **89**, 327–343.

7 L. Jiang, H. Yang, J. K. Yee, X. Mo, T. Topping, E. J. Lavernia and J. M. Schoenung, *Acta Mater.*, 2016, **103**, 128–140.

8 P. V. Liddicoat, X. Z. Liao, Y. Zhao, Y. Zhu, M. Y. Murashkin, E. J. Lavernia, R. Z. Valiev and S. P. Ringer, *Nat. Commun.*, 2010, **1**, 1–7.

9 L. Lu, Y. Shen, X. Chen, L. Qian and K. Lu, *Science (80-.).*, 2004, **304**, 422–426.

10 O. Anderoglu, A. Misra, H. Wang, F. Ronning, M. F. Hundley and X. Zhang, *Appl. Phys. Lett.*, 2008, **93**, 83108.

11 D. Bufford, H. Wang and X. Zhang, *Acta Mater.*, 2011, **59**, 93–101.

12 X. Zhang, A. Misra, H. Wang, T. D. Shen, M. Nastasi, T. E. Mitchell, J. P. Hirth, R. G. Hoagland and J. D. Embury, *Acta Mater.*, 2004, **52**, 995–1002.

13 X. Zhang, A. Misra, H. Wang, M. Nastasi, J. D. Embury, T. E. Mitchell, R. G. Hoagland and J. P. Hirth, *Appl. Phys. Lett.*, 2004, **84**, 1096–1098.

14 D. C. Bufford, Y. M. Wang, Y. Liu and L. Lu, *MRS Bull.*, 2016, **41**, 286–291.

15 L. Lu, X. Chen, X. Huang and K. Lu, *Science (80-.).*, 2009, **323**, 607.

16 D. Bufford, Z. Bi, Q. X. Jia, H. Wang and X. Zhang, *Appl. Phys. Lett.*, 2012, **101**, 223112.

17 J. Wang, F. Sansoz, J. Huang, Y. Liu, S. Sun, Z. Zhang and S. X. Mao, *Nat. Commun.*, 2013, **4**, 1742.

18 O. Anderoglu, A. Misra, H. Wang and X. Zhang, *J. Appl. Phys.*, 2008, **103**, 94322.

19 X. Zhang and A. Misra, *Scr. Mater.*, 2012, **66**, 860–865.

20 Z.-H. Jin, P. Gumbsch, K. Albe, E. Ma, K. Lu, H. Gleiter and H. Hahn, *Acta Mater.*, 2008, **56**, 1126–1135.

21 J. R. Greer, *Nat. Mater.*, 2013, **12**, 689–690.

22 Y. M. Wang, F. Sansoz, T. LaGrange, R. T. Ott, J. Marian, T. W. Barbee, A. V. Hamza, T. W. Barbee Jr and A. V. Hamza, *Nat. Mater.*, 2013, **12**, 697–702.

23 X. Zhang, A. Misra, H. Wang, A. L. Lima, M. F. Hundley and R. G. Hoagland, *J. Appl. Phys.*, 2005, **97**, 94302.

24 N. Li, J. Wang, A. Misra, X. Zhang, J. Y. Huang and J. P. Hirth, *Acta Mater.*, 2011, **59**, 5989–5996.

25 J. Wang, O. Anderoglu, J. P. Hirth, A. Misra and X. Zhang, *Appl. Phys. Lett.*, 2009, **95**, 93–96.

26 R. Niu and K. Han, *Scr. Mater.*, 2013, **68**, 960–963.

27 E. Ma, Y. M. Wang, Q. H. Lu, M. L. Sui, L. Lu and K. Lu, *Appl. Phys. Lett.*, 2004, **85**, 4932–4934.

28 X. H. Chen and L. Lu, *Scr. Mater.*, 2007, **57**, 133–136.

29 J. H. Lee, T. B. Holland, A. K. Mukherjee, X. Zhang and H. Wang, *Sci. Rep.*, 2013, **3**,

1061.

30 D. Bufford, Y. Liu, J. Wang, H. Wang and X. Zhang, *Nat. Commun.*, 2014, **5**, 4864.

31 O. Anderoglu, A. Misra, J. Wang, R. G. Hoagland, J. P. Hirth and X. Zhang, *Int. J. Plast.*, 2010, **26**, 875–886.

32 M. Chen, E. Ma, K. J. Hemker, H. Sheng, Y. Wang and X. Cheng, *Science (80-.).*, 2003, **300**, 1275–1277.

33 X. Z. Liao, F. Zhou, E. J. Lavernia, D. W. He and Y. T. Zhu, *Appl. Phys. Lett.*, 2003, **83**, 5062–5064.

34 F. Zhao, L. Wang, D. Fan, B. X. Bie, X. M. Zhou, T. Suo, Y. L. Li, M. W. Chen, C. L. Liu, M. L. Qi, M. H. Zhu and S. N. Luo, *Phys. Rev. Lett.*, 2016, **116**, 1–5.

35 S. Xue, Z. Fan, O. B. Lawal, R. Thevamaran, Q. Li, Y. Liu, K. Y. Yu, J. Wang, E. L. Thomas, H. Wang and X. Zhang, *Nat. Commun.*, 2017, **8**, 1–9.

36 S. B. Jin, K. Zhang, R. Bjørge, N. R. Tao, K. Marthinsen, K. Lu and Y. J. Li, *Appl. Phys. Lett.*, 2015, **107**, 1–5.

37 D. Bufford, Y. Liu, Y. Zhu, Z. Bi, Q. X. Jia, H. Wang and X. Zhang, *Mater. Res. Lett.*, 2013, **1**, 51–60.

38 S. Xue, Z. Fan, Y. Chen, J. Li, H. Wang and X. Zhang, *Acta Mater.*, 2015, **101**, 62–70.

39 S. Xue, W. Kuo, Q. Li, Z. Fan, J. Ding, R. Su, H. Wang and X. Zhang, *Acta Mater.*, 2018, **144**, 226–234.

40 Q. Li, S. Xue, J. Wang, S. Shao, A. H. Kwong, A. Giwa, Z. Fan, Y. Liu, Z. Qi, J. Ding, H.

Wang, J. R. Greer, H. Wang and X. Zhang, *Adv. Mater.*, , DOI:10.1002/adma.201704629.

41 B. S. Lim, A. Rahtu and R. G. Gordon, *Nat. Mater.*, 2003, **2**, 749–754.

42 Y. J. Lee and S.-W. Kang, *J. Vac. Sci. Technol. A Vacuum, Surfaces, Film.*, 2002, **20**, 1983.

43 Y. J. Lee and S.-W. Kang, *Electrochem. Solid-State Lett.*, 2002, **5**, C91.

44 T. Y. Huang, C. J. Marvel, P. R. Cantwell, M. P. Harmer and C. A. Schuh, *J. Mater. Sci.*, 2015, **51**, 438–448.

45 W.-H. Kim, H.-B.-R. Lee, K. Heo, Y. K. Lee, T.-M. Chung, C. G. Kim, S. Hong, J. Heo and H. Kim, *J. Electrochem. Soc.*, 2011, **158**, D1.

46 H.-B.-R. Lee and H. Kim, *Electrochem. Solid-State Lett.*, 2006, **9**, G323.

47 S.M. George, *Chem. Rev.*, 2010, **110**, 111.

48 X. L. Wu, M. X. Yang, F. P. Yuan, L. Chen and Y. T. Zhu, *Acta Mater.*, 2016, **112**, 337–346.

49 G.-D. Sim, J. A. Krogstad, K. M. Reddy, K. Y. Xie, G. M. Valentino, T. P. Weihs and K. J. Hemker, *Sci. Adv.*, 2017, **3**, e1700685.

50 G. M. Pharr and W. C. Oliver, *MRS Bull.*, 1992, **17**, 28–33.

51 A. T. Jennings, M. J. Burek and J. R. Greer, *Phys. Rev. Lett.*, 2010, **104**, 1–4.

52 D. Jang, X. Li, H. Gao and J. R. Greer, *Nat. Nanotechnol.*, 2012, **7**, 594–601.

53 J. R. Greer and J. T. M. De Hosson, *Prog. Mater. Sci.*, 2011, **56**, 654–724.

54 C. A. Volkert and E. T. Lilleodden, *Philos. Mag.*, 2006, **86**, 5567–5579.

55 H. Zhang, B. E. Schuster, Q. Wei and K. T. Ramesh, *Scr. Mater.*, 2006, **54**, 181–186.

56 M. Mata, M. Anglada and J. Alcalá, *J. Mater. Res.*, 2002, **17**, 964–976.

57 Y. F. Zhang, S. Xue, Q. Li, C. Fan, R. Su, J. Ding, H. Wang, H. Wang and X. Zhang, *Scr. Mater.*, 2018, **148**, 5–9.

58 M. F. Doerner, D. S. Gardner and W. D. Nix, *J. Mater. Res.*, 1986, **1**, 845–851.

59 K. V Rajulapati, R. O. Scattergood, K. L. Murty, G. Duscher and C. C. Koch, *Scr. Mater.*, 2006, **55**, 155–158.

60 X. K. Sun, H. T. Cong, M. C. Yang and M. Sun, *Metall. Mater. Trans. A*, 2000, **31**, 1017–1024.

61 M. H. Shaeri, M. T. Salehi, S. H. Seyyedein, M. R. Abutalebi and J. K. Park, *Mater. Des.*, 2014, **57**, 250–257.

62 M. Y. Murashkin, A. R. Kil'mametov and R. Z. Valiev, *Phys. Met. Metallogr.*, 2008, **106**, 90.

63 S. Xue, Z. Fan, O. B. Lawal, R. Thevamaran, Q. Li, Y. Liu, K. Y. Yu, J. Wang, E. L. Thomas and H. Wang, *Nat. Commun.*, 2017, **8**, 1653.

64 J. Wang, N. Li, O. Anderoglu, X. Zhang, A. Misra, J. Y. Huang and J. P. Hirth, *Acta Mater.*, 2010, **58**, 2262–2270.

65 J. Hu, Y. N. Shi, X. Sauvage, G. Sha and K. Lu, *Science (80-.).*, 2017, **355**, 1292–1296.

66 T. J. Rupert, J. C. Trenkle and C. A. Schuh, *Acta Mater.*, 2011, **59**, 1619–1631.

67 G. P. M. Leyson, W. A. Curtin, L. G. Hector and C. F. Woodward, *Nat. Mater.*, 2010, **9**, 750–755.

68 K. Ma, H. Wen, T. Hu, T. D. Topping, D. Isheim, D. N. Seidman, E. J. Lavernia and J. M. Schoenung, *Acta Mater.*, 2014, **62**, 141–155.

69 R. L. Fleischer, *Acta Metall.*, 1962, **10**, 835–842.

70 A. M. Minor, S. A. S. Asif, Z. Shan, E. A. Stach, E. Cyrankowski, T. J. Wyrobek and O. L. Warren, *Nat. Mater.*, 2006, **5**, 697.

71 M. A. Meyers, A. Mishra and D. J. Benson, *Prog. Mater. Sci.*, 2006, **51**, 427–556.

72 J. R. Trelewicz and C. A. Schuh, *Acta Mater.*, 2007, **55**, 5948–5958.

73 T. J. Rupert, D. S. Gianola, Y. Gan and K. J. Hemker, *Science*, 2009, **326**, 1686–1690.

74 Z. W. Shan, E. a Stach, J. M. K. Wiezorek, J. a Knapp, D. M. Follstaedt and S. X. Mao, *Science*, 2004, **305**, 654–657.

75 X. Z. Liao, F. Zhou, E. J. Lavernia, S. G. Srinivasan, M. I. Baskes, D. W. He and Y. T. Zhu, *Appl. Phys. Lett.*, 2003, **83**, 632–634.

76 H. Van Swygenhoven, P. M. Derlet and A. Hasnaoui, *Phys. Rev. B*, 2002, **66**, 024101.

77 O. Anderoglu, A. Misra, J. Wang, R. G. Hoagland, J. P. Hirth and X. Zhang, *Int. J. Plast.*, 2010, **26**, 875–886.

78 H. Idrissi, B. Wang, M. S. Colla, J. P. Raskin, D. Schryvers and T. Pardoen, *Adv. Mater.*, 2011, **23**, 2119–2122.

79 I. J. Beyerlein, X. Zhang and A. Misra, *Annu. Rev. Mater. Res.*, 2014, **44**, 329–363.

80 X. Zhang, O. Anderoglu, R. G. Hoagland and A. Misra, *Jom*, 2008, **60**, 75–78.

81 N. Izyumskaya, Y. I. Alivov, S. J. Cho, H. Morkoç, H. Lee and Y. S. Kang, *Crit. Rev. Solid State Mater. Sci.*, 2007, **32**, 111–202.

82 J. Wang, A. Misra and J. P. Hirth, *Phys. Rev. B*, 2011, **83**, 64106.

83 C. C. Koch, R. O. Scattergood, K. A. Darling and J. E. Semones, *J. Mater. Sci.*, 2008, **43**, 7264–7272.

84 J. F. Nie, Y. M. Zhu, J. Z. Liu and X. Y. Fang, *Science (80-.).*, 2013, **340**, 957–960.

85 K. Lücke and K. Detert, *Acta Metall.*, 1957, **5**, 628–637.

86 V. Borovikov, M. I. Mendelev and A. H. King, *Philos. Mag.*, 2014, **94**, 2875–2885.

87 W. A. Soer, J. T. M. De Hosson, A. M. Minor, J. W. Morris Jr and E. A. Stach, *Acta Mater.*, 2004, **52**, 5783–5790.

88 X. Z. Jin Li, D. Y. Xie, S. Xue, C. Fan, Y. Chen, H. Wang, J. Wang, *Acta Mater.*

89 T. Ungár, L. Li, G. Tichy, W. Pantleon, H. Choo and P. K. Liaw, *Scr. Mater.*, 2011, **64**, 876–879.

90 L. Kunz, P. Lukáš and M. Svoboda, *Mater. Sci. Eng. A*, 2006, **424**, 97–104.

91 A. Vinogradov, V. Patlan, Y. Suzuki, K. Kitagawa and V. I. Kopylov, *Acta Mater.*, 2002, **50**, 1639–1651.

92 E. A. El-Danaf, M. S. Soliman, A. A. Almajid and M. M. El-Rayes, *Mater. Sci. Eng. A*, 2007, **458**, 226–234.

93 W. Wei, K. X. Wei and G. J. Fan, *Acta Mater.*, 2008, **56**, 4771–4779.

List of figures

Supplementary materials

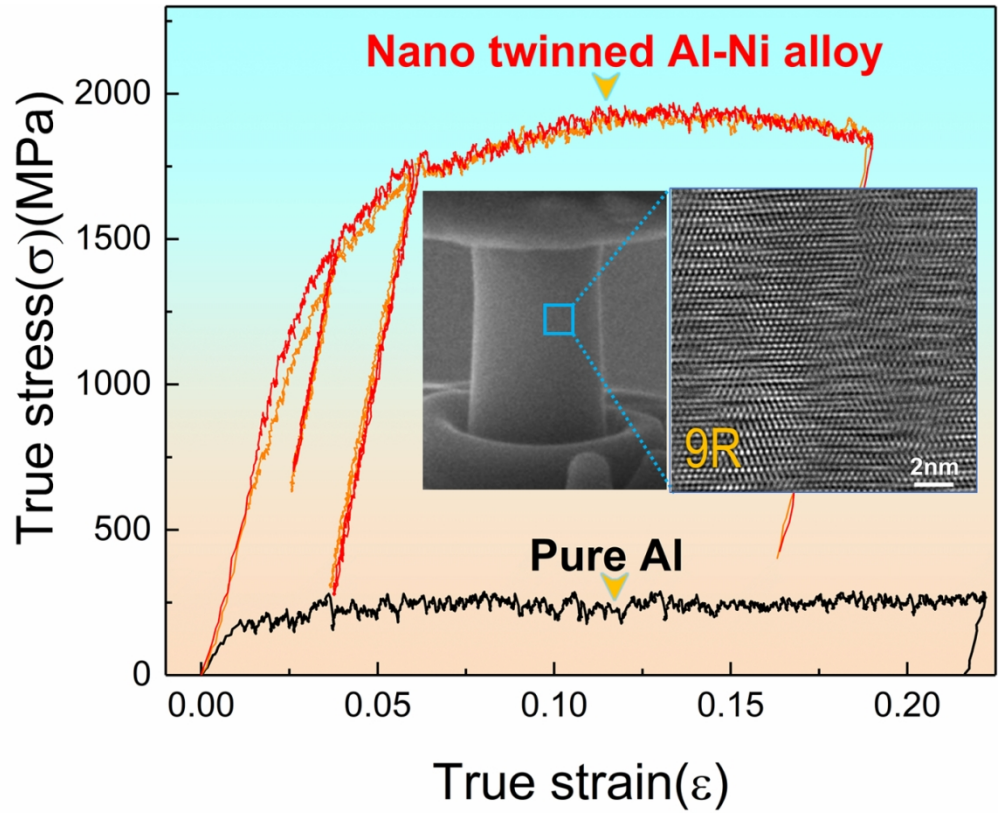

235x190mm (149 x 149 DPI)